Nanoscale

ROYAL SOCIETY
OF **CHEMISTRY**

PAPER
Beatriz Jurado-Sánchez, Alberto Escarpa *et al.*
Photoresponsive MoS₂ and WS₂ microflakes as mobile
biocide agents

NCNST

Photoresponsive MoS₂ and WS₂ microflakes as mobile biocide agents†

Víctor de la Asunción-Nadal, [ID] ‡[a] Javier Bujalance-Fernández, [ID] ‡[a] Beatriz Jurado-Sánchez [ID] *[a,b] and Alberto Escarpa [ID] *[a,b]

A fuel-free strategy for the eradication of *Escherichia coli* and *Staphylococcus aureus* biofilms using WS₂ and MoS₂ photophoretic microflakes is described. The microflakes were prepared by liquid-phase exfoliation of the materials. Under electromagnetic irradiation at 480 or 535 nm, the microflakes experience a fast collective behavior at speeds of over 300 μm s⁻¹ due to photophoresis. Simultaneously to their motion, reactive oxygen species are generated. The fast microflake schooling into multiple moving swarms results in a highly efficient "collision" platform that disrupts the biofilm, enhancing radical oxygen species' contact with the bacteria for their inactivation. As such, removal biofilm mass rates of over 90% and 65% are achieved using the MoS₂ and WS₂ microflakes in the treatment of Gram-negative *E. coli* and Gram-positive *S. aureus* biofilms after 20 min. Much lower removal biofilm mass rates (30%) are obtained under static conditions, revealing the crucial role of microflake movement and radical generation in the active eradication of biofilms. Much higher removal efficiencies are observed in biofilm deactivation as compared with the use of free antibiotics, which are not able to destroy the densely packed biofilms. The new moving microflakes hold considerable promise for the treatment of antibiotic-resistant bacteria.

Introduction

Antimicrobial resistance (AMR) is considered to be one of the major threats worldwide, causing up to 6 million deaths every year.[1–3] Specifically, bacterial biofilms are one of the key issues to tackle in the battle against AMR. In such a particular environment, bacteria can encapsulate into a hydrated layer composed of extracellular polymer substances (EPS) and proteins, generating such biofilms.[4,5] Thus, the access to antibiotics for adequate treatment is hampered[6] but, most importantly, it can be an additional source of AMR bacteria by a horizontal transfer of antibiotic resistance genes among the different bacteria present.[7] As such, it is of paramount importance to develop new strategies for highly efficient biofilm eradication. The high towing force of micromotors (MM), along with their capability to reach hardly accessible areas, make them promising candidates for the treatment of bacterial biofilms.[8–11,12]

To increase biocompatibility and avoid the use for the supply of harsh external chemicals such as hydrogen peroxide, MM designs based on reactive particles have been proposed. For example, clarithromycin-loaded Mg MM[13] or Ga/Zn MM can propel gastric acid for the treatment of *H. pylori* biofilms in the stomach.[13,14] Yet, the limited lifetime associated with the dissolution of reactive Mg or Zn prevents their application in severe infection cases caused by dense biofilms. As an alternative, urease-driven silica MM modified with antibacterial lysozymes exhibits efficient motion in NaHCO₃- and NH₃-rich media for the inactivation of urinary tract *E. coli*-associated biofilms.[15] Additionally, biohybrid magnetotactic *Magnetosopirrillum gryphiswalense* MM have been coated with ciprofloxacin-loaded mesoporous silica for localized delivery into *E. coli* biofilms.[16] Similarly, Pumera's group employed sperm from *Clarias gariepinus* as a MM for direct physical disruption and inactivation of *E. coli* and *S. aureus* biofilms.[17] Still, the above-mentioned biohybrid MM-based configurations require either external fuels or a living organism for actuation, thus raising concerns in terms of biocompatibility and applicability. Alternatively, fuel-free magnetic Ga–Fe liquid metals controlled *via* magnetic fields can physically disrupt both Gram-positive (*S. aureus*) and Gram-negative (*E. coli*) biofilms efficiently.[18] Magnetic Fe₃O₄ MM exhibit a synergetic effect both as a swarm for biofilm physical disruption and hydrogen peroxide decomposition for radical generation.[19] Selective biofilm inactivation has been achieved using ciprofloxacin-

[a]Department of Analytical Chemistry, Physical Chemistry and Chemical Engineering, University of Alcalá, Alcala de Henares, Madrid, E-28805, Spain. E-mail: beatriz.jurado@uah.es, alberto.escarpa@uah.es; Tel: +34 91 8854995
[b]Chemical Research Institute "Andres M. del Rio", University of Alcalá, Alcala de Henares, Madrid, E-28805, Spain
†Electronic supplementary information (ESI) available: Experimental section, supporting figures and supporting videos. See DOI: https://doi.org/10.1039/d3nr00349c
‡These authors contributed equally to this work.

modified magnetic MM prepared using tea leaves[20] or lanbio-tic-modified graphene oxide/Fe$_2$O$_3$ Janus MM.[21] Compared with the vast progress in magnetically propelled MM for biofilm inactivation, a few strategies based on light-driven schemes have been described. For example, ZnO/Ag MM activated with UV light combine autonomous propulsion with the inherent antibacterial properties of the material. Yet, the requirements for hydrogen peroxide as a co-reagent for propulsion hamper the applicability of MM.[22] Thermophoretic NIR-driven mesoporous silica MM coated with gold can inactivate *S. aureus* biofilms in 10 minutes combining localized thermal conversion along with controlled delivery of vancomycin, without damaging surrounding tissues. The latter results indicate the suitability of the combination of photothermal materials with MM for biofilm inactivation.[23]

Transition metal dichalcogenides (TMDs) such as MoS$_2$ and WS$_2$ are promising 2D materials with high photothermal conversion abilities and the so-called quantum confinement effect for interaction with electromagnetic radiation. Such properties have been exploited for the inactivation of bacterial biofilms, either by the photothermal therapy of *S. aureus* under NIR light irradiation,[24] or reactive oxygen species (ROS) production by illumination with VIS and UV light for *E. coli* inactivation.[25] Adequate exfoliation of the material is key to fine-tuning the bandgaps for interaction with electromagnetic radiation and efficient ROS production.[26] In the MM field, TMDs such as MoS$_2$ colloids propelled by self-electrophoretic effects upon UV light action have been used for photolithography purposes.[27] Our group has described the capabilities of WS$_2$/Pt catalytic MM for ROS production upon NIR irradiation.[28]

We have illustrated the light-triggered photophoretic motion of WS$_2$ micromotors prepared by liquid phase exfoliation of the pristine material. The micromotors can move upon VIS light irradiation, reaching a speed of 6000 μm s^{-1}, along with ROS generation.[29] Given the photoconversion abilities of TMDs materials, along with their inherent antibacterial abilities, TMD-based photophoretic microflakes will be explored as an antimicrobial platform. Specifically, we describe the synthesis of photophoretic MoS$_2$ and WS$_2$ microflakes with inherent antibacterial activities for the inactivation of *E. coli* and *S. aureus* biofilms. In the following sections, we will describe the preparation of microflakes from the exfoliation of pristine materials. The microflakes exhibit an efficient motion and swarming behavior upon VIS light irradiation, due mainly to the photothermal properties of the material, and the subsequent heat release and thermal convection. This, in turn, generates a convective fluid flow and efficient propulsion along with the generation of ROS species for bacterial inactivation. As will be illustrated, the high towing force and collective behavior of the microflakes allow for the physical disruption of the biofilm. Alternatively, the generated ROS have a role in bacterial membrane deactivation. The microflakes can inactive *E. coli* and *S. aureus* biofilms in just 20 min after treatment, without the requirements for harsh reagents, or modification with antibiotic drugs, holding considerable promise for the on-demand treatment of bacterial biofilms in environ-mental and water treatment of food safety-related applications, among others. To the best of our knowledge, this is the first time that photophoretic TMD-based microflakes are used for the treatment of bacterial biofilms.

Results and discussion

The concept of photophoretic microflakes for bacterial biofilm inactivation is illustrated in Fig. 1. Upon VIS light irradiation, the microflakes experience a photophoretic swarming behavior. Simultaneously, ROS are generated *via* a reaction with the solvent. Briefly, under irradiation at a suitable energy, electrons can be promoted from the valence band to the conduction band generating electron–hole pairs. The photogenerated electrons can react with O$_2$ molecules in water to produce O$_2^-$ radicals, whereas the positively charged holes can react with the solvent, in this case water, to generate OH$^-$ radicals as follows:[28,30,31]
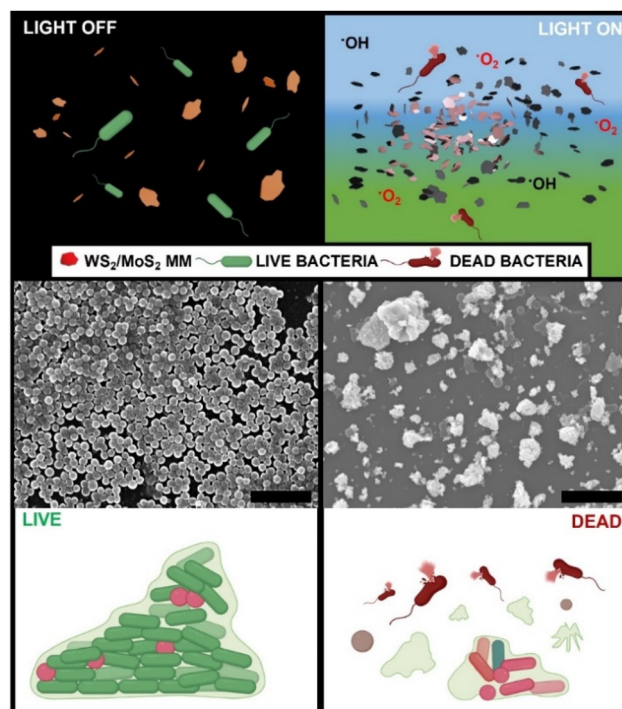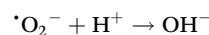
$$WS_2/MoS_2 + h\nu \rightarrow e^- + h^+$$

$$H_2O \rightarrow H^+ + OH^-$$

$$OH^- + h^+ \rightarrow {}^{\bullet}OH$$

$$O_2 + e^- \rightarrow {}^{\bullet}O_2^- \rightarrow {}^1O_2$$

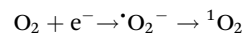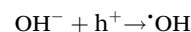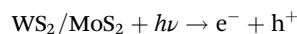$${}^{\bullet}O_2^- + H^+ \rightarrow OH^-$$

Fig. 1 Schematic of photophoretic MoS$_2$ and WS$_2$ microflakes for *E. coli* and *S. aureus* bacterial biofilm eradication. The middle part of the figure shows the SEM images of an *S. aureus* biofilm before and after treatment with WS$_2$ microflakes after irradiation at 535 nm for 20 min. Scale bars, 5 μm.

It is worth noting that the photogenerated radicals are toxic for cells and bacteria, inducing the light-stimulated killing of bacteria and degradation of extracellular polymer substances that compose the biofilm's structure. The synergistic effect of physical and chemical contributions allows for highly efficient biofilm destruction, as reflected in the scanning electron microscopy images (SEM) of a representative *S. aureus* biofilm obtained before and after treatment with WS_2 at 480 nm (blue) irradiation for 20 min

The microflakes are synthesized by controlled exfoliation of the pristine materials in water. The morphology of the as-synthetized microflakes was checked by transmission electron microscopy (TEM), showing irregularly shaped microflakes with an average size of 1 μm (Fig. 2A). Raman spectrometry of the microflakes was also performed, confirming the composition of such particles, and revealing the presence of the A_{1g} and E^1_{2g} phonon modes[32] (Fig. 2B). Finally, X-ray diffraction (XRD) patterns of both materials were recorded (Fig. 2C). All the main bands for WS_2 and MoS_2 were successfully identified, matching the standards reported for these materials in the crystallographic database of the International Centre for Diffraction Data (JCPDS card no. 84-1398 and JCPDS card no. 37-1492, respectively). Hence, from the XRD data, we can confirm that the starting material exhibits good crystallinity without major impurities as well. The average crystallite size was estimated by using Scherrer's equation. The estimated average crystallite size was 11 nm and 65 nm for commercial WS_2 and MoS_2, respectively. SEM characterization and EDX mapping further corroborate the as-observed morphology of the microflakes, with an average diameter of 1.0 ± 0.5 μm and adequate Mo, W, and S distribution (see Fig. S1 in the ESI†). Overall, these data testified to the successful preparation of the microflakes for further experiments regarding their applicability in biofilm disruption.

Before performing the bacterial inactivation experiments, we tested the propulsion behavior and ROS production capabilities of the microflakes, as depicted in Fig. 3. Upon irradiation with VIS light at 480 (blue) or 535 nm (green), the microflakes exhibit a rapid movement and collective behavior as depicted in Fig. 3A, moving at velocities of up to 274 ± 98 (WS_2) or 253 ± 43 μm s^{-1} (MoS_2) in culture media. To characterize the electromagnetic interaction capabilities of the microflakes, UV-VIS spectra were obtained. The direct bandgaps were calculated using the TAUC method, rendering a calculated bandgap of 2.2 eV. As the incident energies are 2.6. eV for 480 nm irradiation and 2.3 eV for 535 nm irradiation, the microflakes can interact with these photons, and electrons are promoted to the conduction band.[33] This can induce self-electrophoretic, self-thermophoretic or photophoretic effects.[34] Please note here that the asymmetry of the system is not given by the geometry of the microflakes but through the application of a radial irradiation gradient. As a result, the microflakes exhibit positive phototactic behavior, moving from less-irradiated areas to more-irradiated areas following a positive phototactic behavior. This type of asymmetry is most common in light-driven micromotors. To gain insights into the propulsion mechanism, we checked the microflake motion in water and in *N,N*-dimethylformamide (DMF). Specifically, DMF was chosen as a non-cleavable solvent to prevent the generation of ROS from water, thus prevent the self-diffusiophoretic motion mechanism. As shown in Fig. 3B, the microflakes move at similar speeds both in water and DMF, revealing that the diffusiophoretic mechanism is not responsible for the observed motion. In a previous study of MoS_2 light-driven micromotors, He *et al.*, identified the MoS_2 photocorrosion as the leading mechanism for the motion of their colloidal micromotors.[27] Main photo corrosion products identified were MoO_3, H$^+$, SO_4^{2-} and Mo^{6+}. The differences in the motion mechanism with our microflakes can be explained, first, considering that our micromotors are larger on average. This has some physico-chemical implications that influence their mobility (*i.e.* enhanced heat retention, high hydrodynamic drag), which altogether may limit the efficiency of a diffusiophoretic mechanism in favor of a heat-exchange mechanism. Second, in the previous article by He *et al.*, the motion is only observed when UV light is irradiated. In contrast, our microflakes can propel efficiently in the entire UV-VIS spectrum. Interestingly, our micromotors can move even at 621 nm, which is below the bandgap and photocorrosion cannot occur. Therefore, while photocorrosion may influence the motion of our microflakes under certain conditions, it cannot be the leading mechanism. It should be noted here that the speed decreases greatly in bacterial culture. Notably, the experiments were performed in the presence of a biofilm. Hence, the drag of the microflakes with the biofilm results in a decrease in the speed. Interestingly,
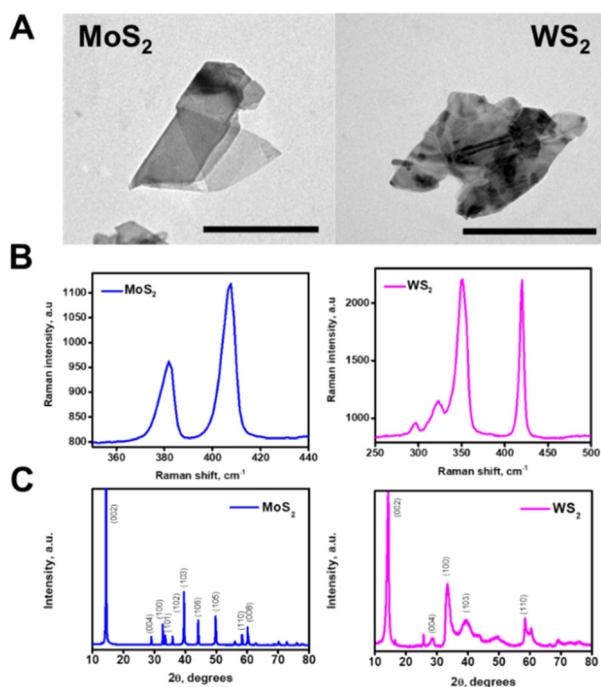

Fig. 2 Characterization of the microflakes. (A) TEM images of the MoS_2 and WS_2 microflakes. (B) Raman spectra of each microflake and (C) XRD patterns of both materials. Scale bars, 500 nm.
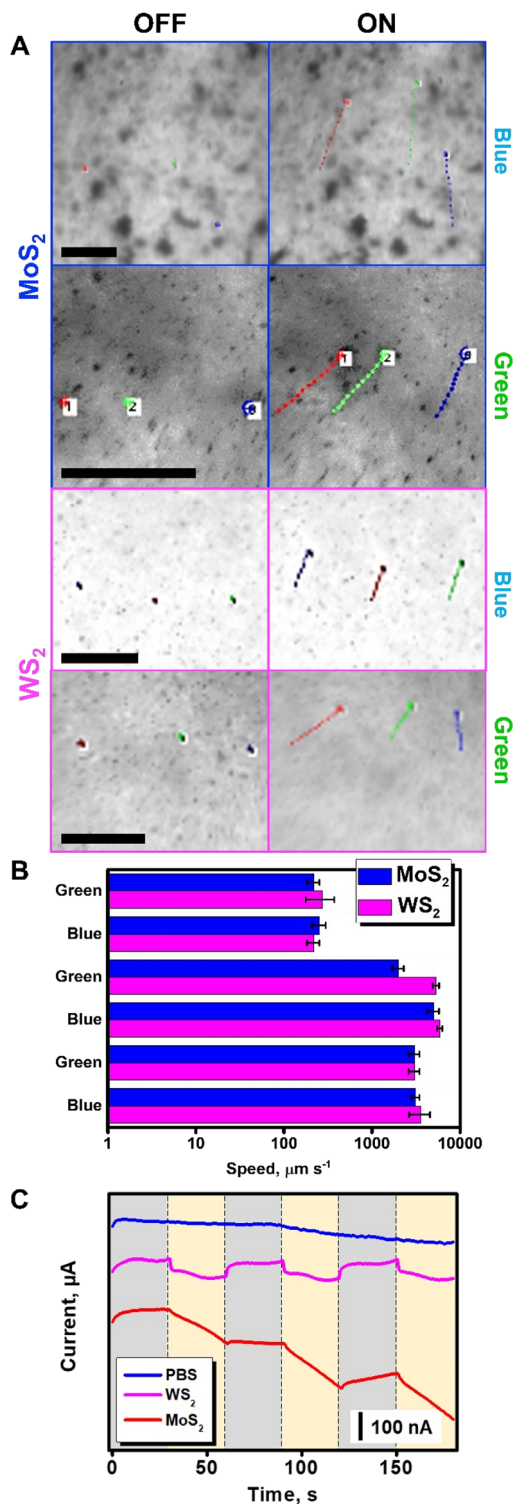
Fig. 3 Characterization of the propulsion of the MoS_2 and WS_2 microflakes in bacterial culture media. (A) Time-lapse images (taken from Video S1†) of the propulsion of MoS_2 and WS_2 microflakes before (OFF) and after irradiation (ON) with electromagnetic radiation at 480 nm (blue) and 535 nm (green) in the presence of an *S. aureus* biofilm with tracking lines. Each point in the line corresponds to 22 ms. (B) Corresponding speed plot in culture media (top), water (middle), and DMF (bottom). (C) Amperometric measurements were performed in PBS, MoS_2, or WS_2 microflake solutions under consecutive cycles of visible light irradiation. Error bars correspond to the standard deviation of 10 measurements. Scale bars, 100 μm.

due to the high efficiency of the TMD-based light-driven microflakes, they can propel at high speeds (above 200 μm s^{-1}) in such a complex medium. Additional control experiments were conducted using graphene oxide flakes as thermophoretic materials with negligible phototactic ability.

As can be seen in Video S1,† no apparent motion of the graphene oxide flakes is observed. This finding indicates that the photophoretic mechanism is the main responsible for the WS_2 and MoS_2 microflake propulsion, as the motion is due to the heat-conversion capabilities of TMD-based flakes. In conclusion, the interaction of incident radiation with the electronic structure of dichalcogenides generates localized heating, which during dissipation renders a hydrodynamic flow responsible for the collective microflake behavior.[35,36] Further details on the propulsion mechanism of photophoretic TMD-based microflakes can be found in the literature with insights into the swarming capabilities of such microflakes and an in-depth study of the interactions between micromotors and the surrounding media.[29] In addition, the holes and vacancies generated in the microflakes are active sites for the reaction with the solvent. Due to the reaction with free electrons and holes, ROS are generated. Furthermore, this reactive species can be further exploited in bacterial degradation, as testified in the amperometric plots in Fig. 3C. In this experiment, solutions containing MoS_2 and WS_2 micromotors in PBS were placed in a transparent ITO electrode and the transient photocurrent was recorded while irradiating the sample in the microscope setup with white light. In this experiment, the photocurrent is related to the separation of charge carriers (electron–hole pairs), which in the case of TMDs is directly related to the generation of ROS. As can be seen, a higher photocurrent was observed for MoS_2, followed by WS_2. As a control, transient photocurrent was not observed in the TMD-free PBS solution.[37]

Once we characterized the motion of the microflakes and the abilities for ROS generation, we tested the abilities for the eradication of *E. coli* and *S. aureus* biofilms as representative Gram-negative and Gram-positive bacteria, respectively. Experiments were performed using both SEM observation and staining with crystal violet (CV) to perform OD_{595} measurement (Fig. 4).

Mature biofilms were grown in 96 multi-well cell culture plates for 48 h as described in the Experimental section in the ESI.† Optical density measurements (OD_{595}) were performed on positive and negative control wells to assess the OD_{595} for blank and viable biofilm on every plate. During a typical biofilm removal experiment, the lysogeny broth (LB) culture medium was removed from each plate, followed by washing with PBS and the addition of the microflakes. To assess the effect of electromagnetic radiation on biofilms containing microflakes, the plates were irradiated for 20 min using a Xe arc lamp, with the optical fiber of an inverted microscope and selecting the desired wavelength (480 or 535 nm). Control experiments were performed without irradiation and keeping the bacteria in contact with the microflakes in the dark. After the treatment, the supernatant with the suspended micro-
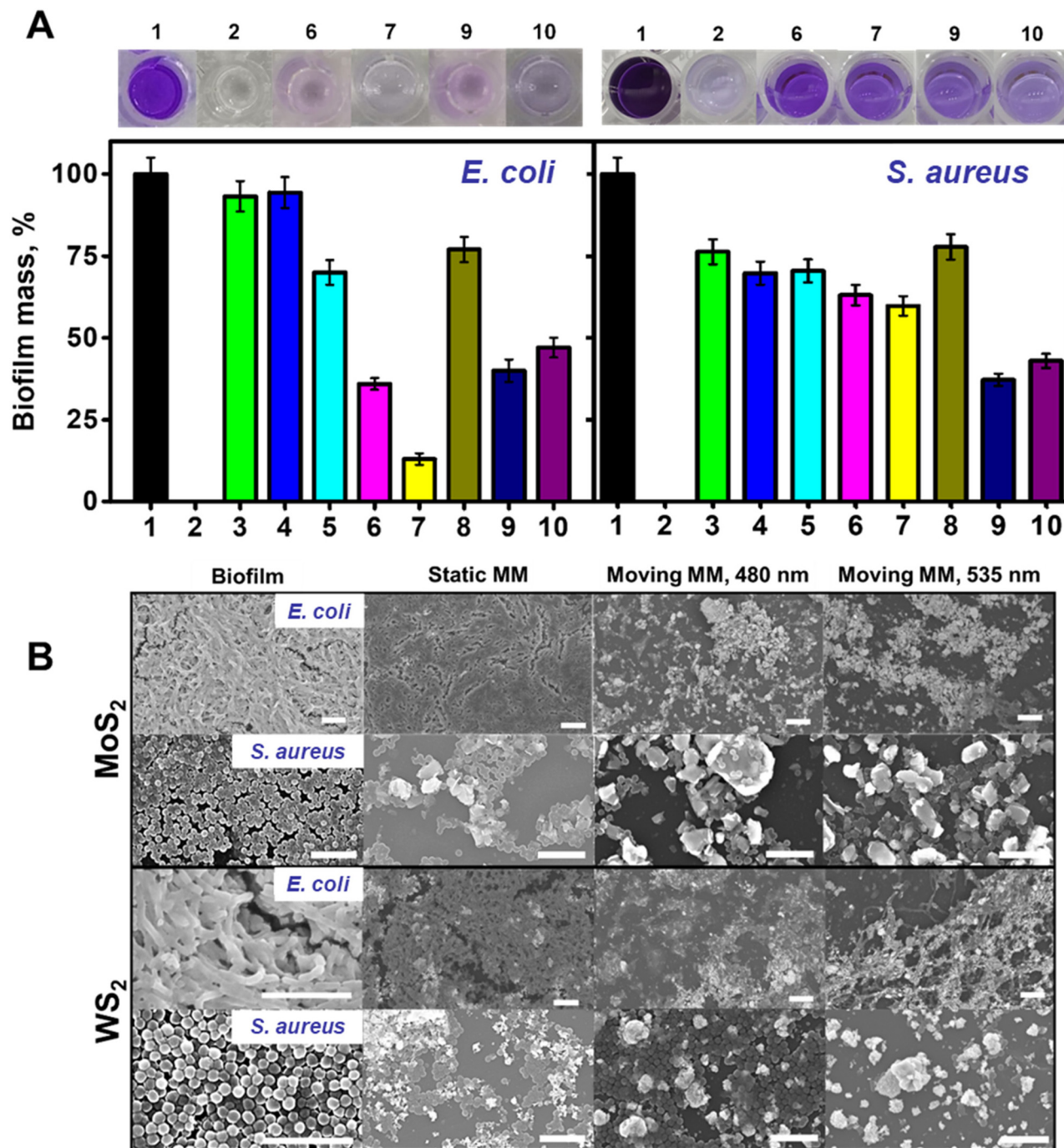
Fig. 4 MoS$_2$ and WS$_2$ microflake-micromotors (MM) for *E. coli* and *S. aureus* biofilm removal. (A) OD$_{595}$ measurements under each condition. The top part shows the images of the plates stained with CV, while the bottom part illustrates the percentage of biofilm mass under different conditions where: (1) initial conditions without MM; (2) control plates with sterile culture media; (3) biofilm growth in the presence of MoS$_2$ MM for 48 h; (4) biofilm growth in the presence of WS$_2$ MM for 48 h; (5) biofilm treated with MoS$_2$ MM in the dark (without electromagnetic irradiation); (6) biofilm treated with MoS$_2$ MM at 480 nm (blue) irradiation for 20 min; (7) biofilm treated with MoS$_2$ MM at 535 nm (green) irradiation for 20 min; (8) biofilm treated with WS$_2$ MM in the dark (without electromagnetic irradiation); (9) biofilm treated with WS$_2$ MM at 480 nm (blue) irradiation for 20 min; and (10) biofilm treated with WS$_2$ MM at 535 nm (green) irradiation for 20 min. (B) Corresponding SEM images of the bacterial biofilms prior, under static, and after treatment with the MM. Error bars correspond to the standard deviation of 3 measurements. Scale bars, 10 μm.

flakes was carefully removed. The remaining biofilm was washed with PBS and fixed with ethanol. To quantify the remaining biofilm and test the ability of the microflakes for its

eradication, 0.1% CV solution was added and left to react for 20 minutes at room temperature. The incubation was then followed by a washing step with PBS. Finally, methanol was

added to solubilize the CV and the obtained solutions were transferred to clean wells for OD_{595} measurements, thus avoiding potential interferences. A decrease in the violet color and, in turn, the OD_{595} value can be related to a higher biofilm removal rate. For further details, please see the Experimental section.†

The data in Fig. 4A illustrate the ability of the WS_2 and MoS_2 microflakes for the efficient removal of both *E. coli* and *S. aureus* biofilms. As the experimental data indicate, different behaviors depending on the type of materials used for different bacterial strains can be observed. Notably, different strains display different morphologies and outer membrane structures, which can affect the ROS interaction mechanism and kinetics. To assess the effect of non-radiated microflakes on biofilm mass, we performed a control experiment in the presence of the microflakes. The results were then represented in terms of % biofilm mass (a low percentage indicates a higher removal rate). In this regard, we added a known amount of microflakes to culture plates during biofilm formation. The obtained results revealed the compatibility of the microflakes with the bacteria, with a percent biofilm formation of 94% for *E. coli* using both materials (bar 3 in Fig. 4A, left and right) and 70–76% for *S. aureus* (bar 4 in Fig. 4A, left and right). These data indicate that the unirradiated material has a negligible effect on bacterial biofilm eradication, thus evidencing the need for ROS generation and physical scarring. Thereafter, we performed bacterial biofilm removal experiments. For *E. coli*, the best removal rate was observed using the MoS_2 microflakes at 535 nm (36 and 13% biofilm masses at 480 and 535 nm, respectively, bars 6 and 7 in Fig. 4A, left), whereas lower removal rates were obtained for the WS_2 microflakes (40 and 47% biofilm masses under irradiation at 480 and 535 nm, respectively, bars 9 and 10 in Fig. 4A, left). In the case of *S. aureus*, the best results were obtained with the WS_2 microflakes, with percentage biofilm masses of 37 and 42%, after 480 and 535 nm irradiation (bars 9 and 10 in Fig. 4A, right) respectively. In the case of MoS_2, biofilm masses are higher, ranging from 63 to 59% after irradiation at 480 and 535 nm (bars 6 and 7 in Fig. 4A, right). Control experiments performed with non-irradiated microflakes (without light irradiation) revealed much lower degradation rates of 77 and 70% for MoS_2 and WS_2 in the treatment of both bacterial strains (bars 5 and 8 on both plots of Fig. 4A), revealing thus the crucial role of microflake motion and ROS production for biofilm inactivation. Furthermore, non-motile MoS_2 and WS_2 (prepared without sonication) were added to both *E. coli* and *S. aureus* biofilms and irradiated. As can be seen in Fig. S2,† the effect on the biofilm mass of irradiated non-motile MoS_2 and WS_2 is less accused than the effect of irradiated microflakes, especially in the case of *E. coli*. These results clearly illustrate the fact that the motion of microflakes plays a leading role in the removal of bacterial biofilms along with the generation of ROS. Negligible biofilm inactivation was observed under 480 or 535 nm light irradiation in the absence of microflakes. These data are fully supported by the SEM images of Fig. 4B, which revealed densely packed biofilms

before the treatment and in the presence of static MM. Nonetheless, after the treatment with microflakes at both wavelengths, biofilm disruption is observed. Particularly, bacterial inactivation is indicated by the shape and disposition of the bacteria. In this regard, the morphological features of the observed treated biofilms contrast with the control. Finally, to discard the effect of temperature on bacterial viability, the temperature was tracked under radiation with both wavelengths using a thermocouple. As the results depicted in Fig. S3† indicate, the heating of the bulk volume is negligible. Certainly, this is in line with the photophoretic mechanism, which explains the motion with localized heating followed by a fast dissipation. Overall, the data obtained for biofilm removal revealed better efficiency for *E. coli* deactivation, with 87% biofilm removal using MoS_2 microflakes at 535 nm. For *S. aureus*, 63% removal rate was obtained while using WS_2 microflakes at 480 nm. Owing to the complexity of bacterial biofilm systems, the analysis of the obtained viabilities is not trivial, as many factors should be considered. Namely: the bacterial outer membrane and type, ROS production and the composition of the microflakes. Regarding bacterial wall, *E. coli* possess an outer membrane composed of lipopolysaccharides and an 8 nm peptidoglycan layer. Gram-positive bacteria, *S. aureus* does not possess an outer membrane but is covered with a thicker peptidoglycan layer of about 80 nm, bounded by covalent linkages. Such a layer imparts the bacteria with a negative net charge, which makes difficult the interactions with negatively charged ROS, such as those produced by our microflakes.[38] Thus, the dominant mechanism for bacterial inactivation is the collision of the microflakes with the cell walls during movement. Bacterial membrane rupture thus allowing for ROS permeation for further inactivation. The thicker peptidoglycan layer (10 times higher in *S. aureus* than in *E. coli*) acts as a protective layer against cell rupture by the action of the microflakes. Overall, these insights into the bacterial cell wall structure can provide a feasible explanation for the slightly lower biofilm inactivation.[39] It is worth noting that the crystal violet stain is not selective to alive bacteria and EPS is also stained.[40] Hence, the results in Fig. 4A should be interpreted as the biofilm mass after treatment and they should not be misinterpreted as bacterial viability.

Additionally, an important aspect of biofilm removal studies is the disruption of extracellular polymer substances (EPS). Specifically, EPS forms a 3D dense network that maintains the biofilm mass and integrity.[21] Thus, the role of the microflakes in EPS disruption was also checked by staining with SYPRO-Ruby red dye. Experiments were performed similarly to that reported for OD_{595} measurements under the best removal rate conditions (see the Experimental section for more details†) and are listed in Fig. 5.

Fluorescence images after SYPRO staining of the biofilm before treatment and under static conditions indicate a high density of proteins in both cases, with an interconnected network. In contrast, a low EPS density was observed after treatment with the microflakes, indicating adequate alteration of the biofilms by collisions during the fast motion and ROS
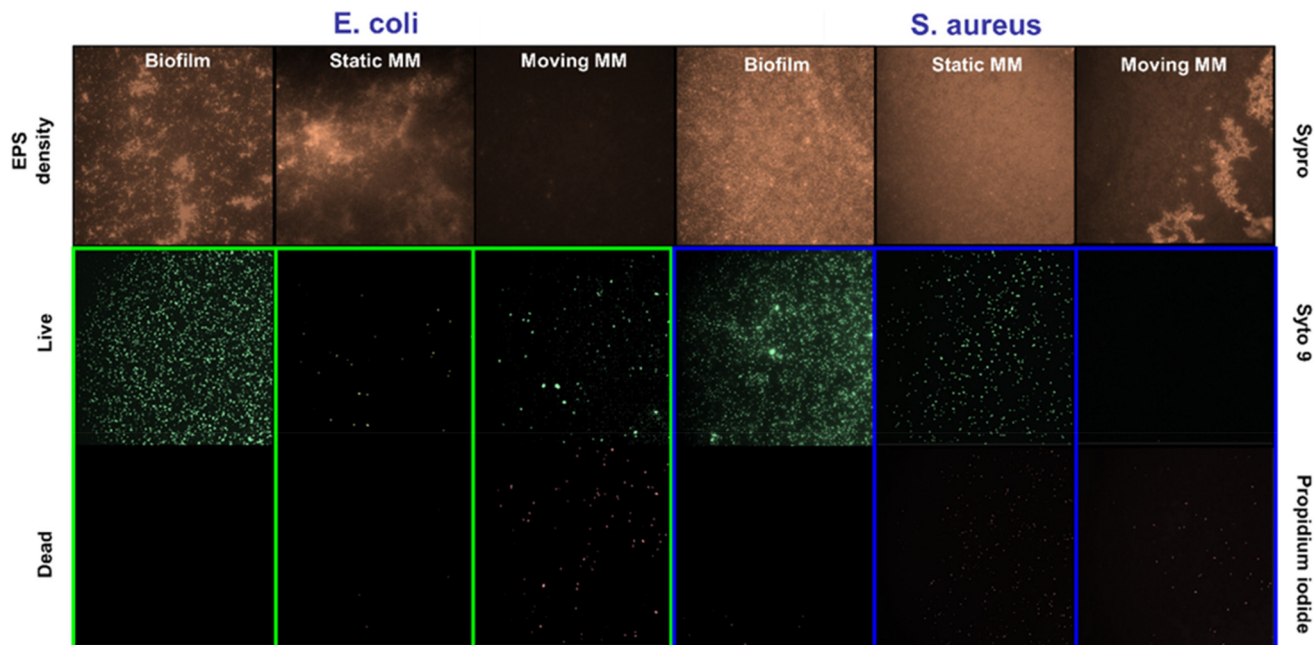
Fig. 5 Effect of the MoS_2 and WS_2 microflake-micromotors (MM) on the EPS of *E. coli* and *S. aureus* biofilms. Fluorescence microscopy images of each biofilm before and after 20 min treatment with MoS_2 microflakes at 535 nm (for *E. coli*) and WS_2 microflakes at 480 nm (for *S. aureus*) using SYPRO-Ruby staining to label the proteins and the LIVE/DEAD stain kit to label the DNA.

generation. We performed additional observation with a commercial LIVE/DEAD staining kit, observing a high density of dead bacteria (as staining with propidium iodide) with moving microflakes, with high viability under static conditions (for further details, see the Experimental section†). Finally, the disruption of the biofilm's structure, allows for the penetration of

Fig. 6 Bacterial viability of *E. coli* and *S. aureus* biofilms with MoS_2 microflakes under 535 nm irradiation and WS_2 microflakes under 480 nm irradiation after the direct administration of an antibiotic drug, and the light-actuated microflakes in the presence of an antibiotic drug. Bacterial viability was estimated using a commercial LIVE/DEAD staining kit and a microplate reader.

antimicrobial agents, further boosting their effects. In this sense, by combining the biofilm disruption capabilities of our light-driven TMD-based microflakes with the administration of an antimicrobial drug, a synergistic effect is expected. In this regard, the dilution of a mixture containing penicillin and streptomycin was evaluated by assessing the evolution of *E. coli* and *S. aureus* cultures in the presence of 1 : 10, 1 : 100, 1 : 1000, and 1 : 10 000 penicillin/streptomycin (Fig. S4†).

Dilutions of 1 : 1000 and 1 : 10 000 were selected for *E. coli* and *S. aureus*, respectively. The effects of the directly administered antibiotic drug, microflakes and antibiotic drug in the presence of microflakes were compared as depicted in Fig. 6. Notably, the microflakes are more efficient for biofilm removal than the use of the antibiotic, as reflected in the bacterial viability percentages reported in Fig. 6. Yet, the synergistic effect between the antibiotic drug and the microflakes results in efficient biofilm inactivation. Overall, the obtained results reveal the suitability of our microflake-based strategy for highly efficient biofilm inactivation without using harsh chemicals or other external inputs for a myriad of environmental or food treatment applications.
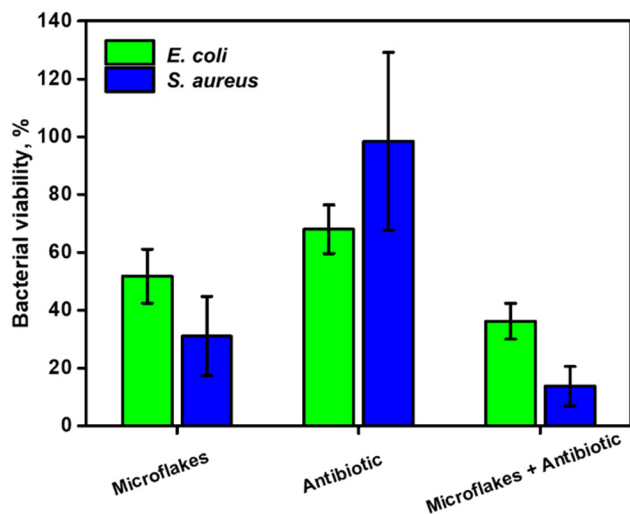
Conclusions

We have reported on a highly antibacterial on-the-fly platform based on photophoretic MoS_2 and WS_2 microflakes driven by the photophoretic effect with remarkable antibacterial properties. Upon VIS light irradiation, the exfoliated materials are locally heated in a photophoretic-based mechanism. This

results in a convective flow that drives the fluid, inducing a schooling behavior of the microflakes into swarms, creating highly efficient "scarring" platforms to disrupt the bacterial biofilms. In addition, the VIS light irradiation interactions on the microflakes result in electron transfer, generating ROS to improve the bacterial killing ability. The effect is complex and is influenced by several factors such as the bacteria's outer membrane and type, ROS production, and composition of the microflakes. Overall, the best conditions for *E. coli* deactivation were found using MoS_2 microflakes at 535 nm with 87% biofilm removal. Alternatively, *S. aureus* exhibits 63% removal rate with WS_2 microflakes at 480 nm, reflecting the influence of peptidoglycan layer thickness, the outer net charge of the microflakes and the morphology. The microflakes can disrupt the EPS of the biofilm, this can be exploited in combination with the administration of antibiotic drugs to increase the biofilm permeability and further enhance the efficiency of such drugs. In this regard, biofilm viabilities of 31% and 23% were observed for *E. coli* and *S. aureus*, respectively. No biofilm deactivation was observed with the use of antibiotics, as those are not able to penetrate the densely packed biofilm. These results prove the applicability of our approach to the disruption and removal of bacterial biofilms, especially in confined spaces.

Author contributions

Víctor de la Asunción-Nadal: conceptualization, data curation, formal analysis, investigation, visualization, and writing – review and editing. Javier Bujalance-Fernández: conceptualization, data curation, formal analysis, investigation, visualization, and writing – review and editing. Beatriz Jurado-Sánchez: conceptualization, formal analysis, funding acquisition, project administration, resources, supervision, writing – original draft, and writing – review and editing. Alberto Escarpa: conceptualization, formal analysis, funding acquisition, project administration, resources, supervision, and writing – review and editing.

Conflicts of interest

There are no conflicts to declare.

Acknowledgements

References

1 C. J. L. Murray, K. S. Ikuta, F. Sharara, L. Swetschinski, L. Robles Aguilar, A. Gray, C. Han, C. Bisignano, P. Rao, E. Wool, S. C. Johnson, A. J. Browne, M. G. Chipeta, F. Fell, S. Hackett, G. Haines-Woodhouse, G. Kashef Hamadani, E. A. P. Kumaran, B. McManigal, R. Agarwal, S. Akech, S. Albertson, J. Amuasi, J. Andrews, A. Aravkin, E. Ashley, F. Bailey, S. Baker, B. Basnyat, A. Bekker, R. Bender, A. Bethou, J. Bielicki, S. Boonkasidecha, J. Bukosia, C. Carvalheiro, C. Castañeda-Orjuela, V. Chansamouth, S. Chaurasia, S. Chiurchiù, F. Chowdhury, A. J. Cook, B. Cooper, T. R. Cressey, E. Criollo-Mora, M. Cunningham, S. Darboe, N. P. J. Day, M. De Luca, K. Dokova, A. Dramowski, S. J. Dunachie, T. Eckmanns, D. Eibach, A. Emami, N. Feasey, N. Fisher-Pearson, K. Forrest, D. Garrett, P. Gastmeier, A. Z. Giref, R. C. Greer, V. Gupta, S. Haller, A. Haselbeck, S. I. Hay, M. Holm, S. Hopkins, K. C. Iregbu, J. Jacobs, D. Jarovsky, F. Javanmardi, M. Khorana, N. Kissoon, E. Kobeissi, T. Kostyanev, F. Krapp, R. Krumkamp, A. Kumar, H. H. Kyu, C. Lim, D. Limmathurotsakul, M. J. Loftus, M. Lunn, J. Ma, N. Mturi, T. Munera-Huertas, P. Musicha, M. M. Mussi-Pinhata, T. Nakamura, R. Nanavati, S. Nangia, P. Newton, C. Ngoun, A. Novotney, D. Nwakanma, C. W. Obiero, A. Olivas-Martinez, P. Olliaro, E. Ooko, E. Ortiz-Brizuela, A. Y. Peleg, C. Perrone, N. Plakkal, A. Ponce-de-Leon, M. Raad, T. Ramdin, A. Riddell, T. Roberts, J. V. Robotham, A. Roca, K. E. Rudd, N. Russell, J. Schnall, J. A. G. Scott, M. Shivamallappa, J. Sifuentes-Osornio, N. Steenkeste, A. J. Stewardson, T. Stoeva, N. Tasak, A. Thaiprakong, G. Thwaites, C. Turner, P. Turner, H. R. van Doorn, S. Velaphi, A. Vongpradith, H. Vu, T. Walsh, S. Waner, T. Wangrangsimakul, T. Wozniak, P. Zheng, B. Sartorius, A. D. Lopez, A. Stergachis, C. Moore, C. Dolecek and M. Naghavi, *Lancet*, 2022, **399**, 629–655.

2 I. Vaz-Moreira, C. Ferreira, O. C. Nunes and C. M. Manaia, in *Antibiotic Drug Resistance*, 2019, pp. 211–238, DOI: **10.1002/9781119282549.ch10**.

3 D. G. J. Larsson and C.-F. Flach, *Nat. Rev. Microbiol.*, 2022, **20**, 257–269.

4 P. S. Stewart and J. W. Costerton, *Lancet*, 2001, **358**, 135–138.

5 H.-C. Flemming, T. R. Neu and D. J. Wozniak, *J. Bacteriol.*, 2007, **189**, 7945–7947.

6 P. Bowler, C. Murphy and R. Wolcott, *Antimicrob. Resist. Infect. Control*, 2020, **9**, 162.

7 I. Michael-Kordatou, P. Karaolia and D. Fatta-Kassinos, *Water Res.*, 2018, **129**, 208–230.

8 J. Wang, *Nanomachines: Fundamentals and Applications*, Wiley, 2013.

9 G. A. Ozin, I. Manners, S. Fournier-Bidoz and A. Arsenault, *Adv. Mater.*, 2005, **17**, 3011–3018.

10 Y. Mei, A. A. Solovev, S. Sanchez and O. G. Schmidt, *Chem. Soc. Rev.*, 2011, **40**, 2109–2119.

11 E. Karshalev, B. Esteban-Fernández de Ávila and J. Wang, *J. Am. Chem. Soc.*, 2018, **140**, 3810–3820.

12 Z. Zhang, L. Wang, T. K. F. Chan, Z. Chen, M. Ip, P. K. S. Chan, J. J. Y. Sung and L. Zhang, *Adv. Healthcare Mater.*, 2022, **11**, 2101991.

13 B. Esteban-Fernández de Ávila, P. Angsantikul, J. Li, M. A. Lopez-Ramirez, D. E. Ramírez-Herrera, S. Thamphiwatana, C. Chen, J. Delezuk, R. Samakapiruk, V. Ramez, M. Obonyo, L. Zhang and J. Wang, *Nat. Commun.*, 2017, **8**, 272.

14 Z. Lin, C. Gao, D. Wang and Q. He, *Angew. Chem., Int. Ed.*, 2021, **60**, 8750–8754.

15 D. Vilela, N. Blanco-Cabra, A. Eguskiza, A. C. Hortelao, E. Torrents and S. Sanchez, *ACS Appl. Mater. Interfaces*, 2021, **13**, 14964–14973.

16 M. M. Stanton, B.-W. Park, D. Vilela, K. Bente, D. Faivre, M. Sitti and S. Sánchez, *ACS Nano*, 2017, **11**, 9968–9978.

17 C. C. Mayorga-Martinez, J. Zelenka, J. Grmela, H. Michalkova, T. Ruml, J. Mareš and M. Pumera, *Adv. Sci.*, 2021, **8**, 2101301.

18 A. Elbourne, S. Cheeseman, P. Atkin, N. P. Truong, N. Syed, A. Zavabeti, M. Mohiuddin, D. Esrafilzadeh, D. Cozzolino, C. F. McConville, M. D. Dickey, R. J. Crawford, K. Kalantar-Zadeh, J. Chapman, T. Daeneke and V. K. Truong, *ACS Nano*, 2020, **14**, 802–817.

19 Y. Dong, L. Wang, K. Yuan, F. Ji, J. Gao, Z. Zhang, X. Du, Y. Tian, Q. Wang and L. Zhang, *ACS Nano*, 2021, **15**, 5056–5067.

20 T. Bhuyan, A. T. Simon, S. Maity, A. K. Singh, S. S. Ghosh and D. Bandyopadhyay, *ACS Appl. Mater. Interfaces*, 2020, **12**, 43352–43364.

21 K. Yuan, B. Jurado-Sánchez and A. Escarpa, *Angew. Chem., Int. Ed.*, 2021, **60**, 4915–4924.

22 M. Ussia, M. Urso, K. Dolezelikova, H. Michalkova, V. Adam and M. Pumera, *Adv. Funct. Mater.*, 2021, **31**, 2101178.

23 T. Cui, S. Wu, Y. Sun, J. Ren and X. Qu, *Nano Lett.*, 2020, **20**, 7350–7358.

24 Y. Zhang, W. Xiu, S. Gan, J. Shan, S. Ren, L. Yuwen, L. Weng, Z. Teng and L. Wang, *Front. Bioeng. Biotechnol.*, 2019, **7**, 218.

25 E. Shang, J. Niu, Y. Li, Y. Zhou and J. C. Crittenden, *Environ. Pollut.*, 2017, **224**, 606–614.

26 S. Pandit, S. Karunakaran, S. K. Boda, B. Basu and M. De, *ACS Appl. Mater. Interfaces*, 2016, **8**, 31567–31573.

27 M. Chen, Z. Lin, M. Xuan, X. Lin, M. Yang, L. Dai and Q. He, *Angew. Chem., Int. Ed.*, 2021, **60**, 16674–16679.

28 V. d. L. Asunción-Nadal, B. Jurado-Sánchez, L. Vázquez and A. Escarpa, *Chem. Sci.*, 2020, **11**, 132–140.

29 V. de la Asunción-Nadal, D. Rojas, B. Jurado-Sánchez and A. Escarpa, *J. Mater. Chem. A*, 2023, **11**, 1239–1245.

30 Z. Wang and B. Mi, *Environ. Sci. Technol.*, 2017, **51**, 8229–8244.

31 T. Fatima, S. Husain and M. Khanuja, *Chem. Eng. J. Adv.*, 2022, **12**, 100373.

32 X. Zhang, X.-F. Qiao, W. Shi, J.-B. Wu, D.-S. Jiang and P.-H. Tan, *Chem. Soc. Rev.*, 2015, **44**, 2757–2785.

33 R. María-Hormigos, B. Jurado-Sánchez and A. Escarpa, *Angew. Chem., Int. Ed.*, 2019, **58**, 3128–3132.

34 J. Wang, Z. Xiong, J. Zheng, X. Zhan and J. Tang, *Acc. Chem. Res.*, 2018, **51**, 1957–1965.

35 Y. Hu, W. Liu and Y. Sun, *ACS Appl. Mater. Interfaces*, 2020, **12**, 41495–41505.

36 B. Dai, J. Wang, Z. Xiong, X. Zhan, W. Dai, C.-C. Li, S.-P. Feng and J. Tang, *Nat. Nanotechnol.*, 2016, **11**, 1087–1092.

37 H. Li, Z. Peng, J. Qian, M. Wang, C. Wang and X. Fu, *ACS Appl. Mater. Interfaces*, 2017, **9**, 28704–28715.

38 T. J. Silhavy, D. Kahne and S. Walker, *Cold Spring Harbor Perspect. Biol.*, 2010, **2**(5), 1–15, DOI: **10.1101/cshperspect.a000414**.

39 Y. N. Slavin, J. Asnis, U. O. Häfeli and H. Bach, *J. Nanobiotechnol.*, 2017, **15**, 65.

40 J. Makovcova, V. Babak, P. Kulich, J. Masek, M. Slany and L. Cincarova, *Microb. Biotechnol.*, 2017, **10**, 819–832.